Published in final edited form as:
Neuroimage. 2011 October 15; 58(4): 984–992. doi:10.1016/j.neuroimage.2011.07.005.

Reconstructing micrometer-scale fiber pathways in the brain: multi-contrast optical coherence tomography based tractography

Hui Wang[a], **Adam J. Black**[a], **Junfeng Zhu**[a], **Tyler W. Stigen**[a], **Muhammad K. Al-Qaisi**[a], **Theoden I. Netoff**[a], **Aviva Abosch**[b], and **Taner Akkin**[a,*]

[a]Department of Biomedical Engineering, University of Minnesota, Minneapolis, MN, USA

[b]Department of Neurosurgery, University of Minnesota, Minneapolis, MN, USA

Abstract

Comprehensive understanding of connective neural pathways in the brain has put great challenges on the current imaging techniques, for which three-dimensional (3D) visualization of fiber tracts with high spatiotemporal resolution is desirable. Here we present optical imaging and tractography of rat brain *ex-vivo* using multi-contrast optical coherence tomography (MC-OCT), which is capable of simultaneously generating depth-resolved images of reflectivity, phase retardance, optic axis orientation and, for *in-vivo* studies, blood flow images. Using the birefringence property of myelin sheath, nerve fiber tracts as small as a few tens of micrometers can be resolved and neighboring fiber tracts with different orientations can be distinguished in cross-sectional optical slices, 2D *en-face* images and 3D volumetric images. Combinational contrast of MC-OCT images enables visualization of the spatial architecture and nerve fiber orientations in the brain with unprecedented detail. The results suggest that optical tractography, by virtue of its direct accessibility to nerve fibers, has the potential to validate diffusion magnetic resonance images and investigate structural connections in normal brain and neurological disorders. In addition, an endoscopic MC-OCT may be useful in neurosurgical interventions to aid in placement of deep brain stimulating electrodes.

Keywords

tractography; optical coherence tomography; polarization; brain imaging; brain connectivity; white matter; gray matter

Introduction

The brain is composed of roughly 100 billion neurons that contain trillions of connective tracts. Despite the progress in understanding operations of single neurons and their functions at the system level, the communicative and cooperative pathways in the axonal networks of the brain remains elusive. Considerable research has been directed toward identifying the pathways of axonal connections between nuclei and cortical layers in recent years.

*Corresponding author. 7-105 Hasselmo Hall, 312 Church Street SE, Minneapolis, MN 55455, USA, akkin@umn.edu (T. Akkin).

Histological methods have contributed in the microscopic anatomy and local tracing of myelinated nerve fibers (Burgel et al, 1997; Burkhalter et al., 1993; Lanciego and Wouterlood, 2000); however, a number of technical challenges limit the study of three-dimensional (3D) architecture and connections of long fiber tracts using two-dimensional (2D) histological images (Lichtman et al., 2008). Diffusion magnetic resonance imaging (MRI) techniques (diffusion tensor imaging and high angular resolution diffusion imaging) utilizing the anisotropic diffusion of water molecules along the fiber tracts have been developed recently to noninvasively study brain connectivity (Basser et al., 1994; Conturo et al., 1999; Tuch et al., 2002). However, the diffusion imaging approach suffers from relatively low spatial resolution (in millimeters), and the nature of probability-based analysis may lead to spurious interpretations of real fiber structures in the brain (Assaf and Pasternak, 2008). Comprehensive understanding of structural connections in the brain requires 3D visualization of fiber tracts with high spatiotemporal resolution.

Optical coherence tomography (OCT) provides depth-resolved cross-sectional images of tissue microstructures with micrometer scale resolution (Huang et al., 1991). The feasibility of using OCT to image the brain has already been demonstrated (Jeon et al., 2006). In the conventional OCT setup, gray matter and white matter are differentiated by their scattering properties. Polarization-sensitive OCT (PS-OCT) (de Boer et al., 1997) utilizes an optical property of the myelin sheath of nerve fibers, known as birefringence (Δn), to determine the spatial organization and orientations of fiber tracts. Birefringence, which is a consequence of the alignment of macromolecular arrays of lipids and proteins contained in myelin (de Campos et al., 1980) results in a single axis of optical anisotropy in each fiber. Birefringence can be quantified by a phase shift, known as phase retardance, between the orthogonal polarization states of polarized light passing through the brain tissue. Orientation of the fiber axis is derived from the optic axis orientation measure that is discussed below. It has been shown that a free-space PS-OCT can be used to differentiate white matter from gray and to determine fiber orientations in *ex-vivo* rat brain in multiple measurements (Nakaji et al., 2008). Fiber tract maps in human postmortem brains have also been constructed using polarized light imaging (Axer et al., 2011). In this method, spatial resolution was defined by the pixel size of the imaging camera and the section thickness of the brain slice. 3D fiber reconstructions were then generated by registering images acquired from serial slices.

In this paper, we use a polarization-maintaining-fiber (PMF) based multi-contrast (MC) OCT system to realize 3D imaging and fiber tractography in *ex-vivo* rat brain. The MC-OCT system, named for the integration of a spectral domain polarization-sensitive OCT (Wang et al., 2010) with Doppler OCT, can generate depth-resolved reflectivity, birefringence/retardance, axis orientation and blood flow images, all simultaneously. The micrometer scale resolution enables visualization of fiber tract architecture with an unprecedented level of detail.

Methods

System description

The construction and characterization of the optical system has been described in our previous paper (Wang et al., 2010). The experimental setup for rat brain imaging is illustrated in Figure 1A. Briefly, light from the source (a near-infrared superluminescent diode, $\lambda_0 = 840\ nm$, $\Delta\lambda = 50\ nm$) is linearly polarized and coupled into one of the orthogonal channels of the PMF. Then, a PMF-based 2 × 2 coupler splits the light into the reference and sample arms of the interferometer. In the reference arm, a quarter-wave plate (QWP) is oriented at 22.5° with respect to the incoming polarization state. As a result, the returning light becomes 45° linearly polarized and couples back into PMF channels equally. In the sample arm, another QWP oriented at 45° ensures circularly polarized light incident on the

sample. Light interacts with anisotropic tissues and the polarization state is altered to an elliptical state due to tissue birefringence. Therefore, back scattered or reflected light is coupled into the PMF channels. The waves from the sample and reference arms are then combined in the 2 × 2 coupler and their interference is acquired in the detection arm of the interferometer. After passing through a transmission grating, the orthogonal polarization states of the light spectrum are laterally split by a Wollaston prism, and finally focused on a line scan CCD camera. Oscillations on the spectra yield information along the depth (z-axis) profile. During the experiment, the incident beam is laterally scanned over the sample in two dimensions (xy plane) allowing for 3D reconstruction of the tissue sample. This system can generate multiple contrasts—reflectivity, phase retardance and axis orientation – simultaneously along a depth profile (A-line) from a single scan (Wang et al., 2010). Doppler shift is another available contrast that can be used to visualize blood flow and blood vessels for *in-vivo* studies. The depth resolution is about 5.4 μm in tissue (with a refractive index of 1.4), and the lateral resolution is about 15 μm. The system has a sensitivity of 98.6 dB for reflectivity measurements.

Sample preparation and imaging

A healthy adult rat brain was obtained from the Tissue Sharing Program after approval by the Research Animal Resources at the University of Minnesota. The brain was fixed in 10% buffered formalin for 48 hours prior to imaging. Myelin sheath integrity in postmortem brain tissue is not affected by proper fixation (de Campos et al., 1980). After fixation, one hemisphere of the brain was glued to a metal plate with the sagittal plane (xy plane) facing upward, and submerged in saline. The preparation was then mounted on a Vibratome (Leica Microsystems, Bannockburn, IL), which was placed under the sample arm of MC-OCT for imaging (Figure 1B). The incident power on the sample was 3.9 mW. With an optical scanning angle of ±6°, the imaging area covered a field of view of 6.25 × 6.25 mm^2. Each cross-sectional image contained 1000 A-lines, and 250 cross-sections (frames) were acquired at 20 fps for 3D imaging. Each A-line contained 512 points with 3.4 μm spacing. Therefore, each voxel spanned a tissue volume of 6.25 × 25 × 3.4 μm^3. After one volume scan, a 500-μm brain section was removed using the Vibratome, allowing deeper regions to be imaged for a new section. A total of twelve scans were performed over the hemisphere. Afterwards, the brain slices were imaged using a conventional microscope for comparison.

Data analysis

Cross-sectional image reconstruction and signal analysis—Several steps need to be performed to reconstruct the image from the recorded spectra: data in wavelength-space are remapped and interpolated in *k*-space (Dorrer et al., 2000), dispersion imbalance is compensated (Cense et al., 2004), the background from the reference arm is subtracted (Leitgeb et al., 2003), and finally an inverse Fourier transform is applied to obtain the complex depth profiles, which are expressed in the form of $A_{1,2}(z)exp\{i\Phi_{1,2}(z)\}$, where A and Φ denote the amplitude and phase, respectively, along the depth z, and the subscripts correspond to the orthogonal polarization channels of the PMF. Reflectivity $R(z)$, phase retardance $\delta(z)$ and relative optic axis orientation $\theta(z)$ are extracted as (Götzinger et al., 2005),

$$R(z) \propto A_1(z)^2 + A_2(z)^2 \quad (1)$$

$$\delta(z) = \arctan(A_1(z)/A_2(z)) \quad (2)$$

$$\theta(z)=(\varphi_1(z)-\varphi_2(z))/2. \quad (3)$$

Flow is calculated from amplitude-weighted Doppler shift on phase signals (Park et al., 2005), and expressed as below. Although flow information is only available for *in-vivo* imaging, we mention it here for future applications.

$$\omega(z)=\frac{1}{T}\frac{A_1^2(z)\Delta\Phi_1(z)+A_2^2(z)\Delta\Phi_2(z)}{A_1^2(z)+A_2^2(z)} \quad (4)$$

where $\Delta\Phi_{1,2}(z)=\Phi^{(n)}{}_{1,2}(z)-\Phi^{(n-1)}{}_{1,2}(z)$, *n* and *n-1* denoting two consecutive A-lines, and *T* is the time interval between the A-lines.

Cross-sectional images are generated by stacking 1000 A-lines acquired during lateral scanning (x-axis). Reflectivity represents the scattering properties of the tissue. Phase retardance indicates the presence of anisotropic tissue with an optic axis, and the birefringence Δn can be characterized by the derivative of retardance along the axial (z) direction as

$$\Delta n(z)=(\lambda/2\pi)\cdot\frac{d\delta(z)}{dz}. \quad (5)$$

It should be noted that the measured phase retardance is also dependent on the inclination angle between the tissue axis and the wave oscillation plane (Larsen et al., 2007). Therefore, the value calculated from Eq. (5) is apparent birefringence.

Optic axis orientation, also called in-plane orientation, represents the angle of the axis of tissue anisotropy on the oscillation plane of the incident wave with respect to a reference axis. Due to an arbitrary phase delay between the PMF channels, our system determines a relative optic axis orientation across lateral scans.

In order to quantitatively evaluate the differentiability of white matter and gray matter using MC-OCT images, features were extracted from the reflectivity and retardance images. Collimated light attenuates exponentially with depth according to the Beer-Lambert law. The light attenuation in tissue can be quantified by the slope of the logarithmic reflectivity in the axial direction (A-line), provided that the beam is not tightly focused. Another feature is derived from the slope of retardance, which represents the apparent birefringence of the A-line. A linear least-squares fit is applied to obtain the slopes of logarithmic reflectivity and phase retardance. An unpaired student's *t*-test was used to determine if the feature differences between white matter and gray matter were significant.

En-face imaging—Integration or maximum projection of the depth information has been used to produce *en-face* image, which is a 2D projection of a 3D OCT dataset. We reconstructed *en-face* images for each MC-OCT contrast, and correlated the results with the bright field images of the brain slice from the microscope. Four pre-processing steps are performed on each cross-sectional image to improve the image quality. First, the reflectivity image is used to exclude the low signal-to-noise ratio (SNR) (< 6) areas. Then, a median filter is applied to reduce the speckle noise. Next, segmentation is used to identify the tissue region. This enables removal of artifacts (e.g. water-air interface and auto-correlation terms)

located outside the imaging area. Finally, an edge detector (Canny, 1986) is used to determine the tissue surface. The pixel intensity $\bar{I}(i, j)$ of the *en-face* images is calculated from these processed/masked images by taking the mean value on each A-line, and is expressed as

$$\bar{I}(i, j)=\frac{1}{N_{i,j}}\sum_{k=1}^{N_{i,j}} S(i, j, k), \tag{6}$$

where $S(i, j, k)$ represents a 3D data set for reflectivity, retardance or axis orientation, i and j are the indices for lateral coordinates and k is the index for axial direction, and $N_{i, j}$ is the number of unmasked (non-zero) elements along depth at the specified (i, j) location. Data was interpolated along the y-axis to maintain the aspect ratio of the 2D image. As a result, *en-face* images of reflectivity, phase retardance and optic axis orientation are reconstructed to facilitate the structure identification and perform comparisons with standard microscope images. Finally, 2D tractography is built up by combining the *en-face* phase retardance and the axis orientation maps, and is displayed in HSV color space. Orientation and retardance maps are encoded as hue and brightness, respectively.

Three-dimensional fiber localization and tracking—The 3D localization of fiber bundles is obtained by utilizing the cross-sectional phase retardance images. The presence of fibers is revealed by an accumulative phase retardance, which increases with depth when light passes through the white matter, compared with no detectable or negligible change in the gray matter. Therefore, the depth localization of the nerve fibers can be achieved by using the birefringence contrast. The local slope of phase retardance is quantified by taking the numerical difference between two neighboring retardance values along depth (Stifter et al., 2010). Since speckle noise significantly affects the differential calculation, we eliminated the speckle through three steps. First, a 4 × 4 moving average filter is applied over the lateral (xy) plane. Then an adaptive nonlinear diffusion filter (Perona and Malik, 1990; Cattéet al., 1992) was performed on cross-sectional images. The purpose of the nonlinear diffusion filter is to further reduce the speckle noise while preserving the edge of the features. Finally, a “spline” smoothing algorithm was applied to eliminate the local fluctuations on the A-lines. After the speckle de-noising, the numerical difference of retardance along the depth profile was computed, and a birefringence threshold was set to mask the gray matter areas. In addition, we used histogram equilibrium and binary conversion algorithm on the *en-face* phase retardance image to identify A-lines that do not exhibit birefringence. Masking those A-lines further improved the result. We combined the birefringence (Eq. 5) and axis orientation (Eq. 3) information for locating and tracking fibers in 3D space. The 3D tractography is constructed in HSV color space, where axis orientation and birefringence of the fiber tracts are used.

Results

Differentiation of white matter and gray matter

White matter and gray matter exhibit distinct optical properties that allow visualization of nerve fiber tracks by MC-OCT. Figure 2A illustrates a microscopy sagittal section of the right hemisphere, in which white matter appears bright white. The dashed red lines indicate two B-lines (i and ii), where cross-sections are displayed by MC-OCT contrasts in Figure 2B–D. The reflectivity images in Figure 2B suggest that white matter, in general, has a higher peak scattering signal (bright colors) than gray matter, and a sharp decay with depth due to increased attenuation of light. On the other hand, the gray color regions indicate that

gray matter has a deeper penetration and slower attenuation. The left side of the cross-section (i) with highly scattering spots in the reflectivity image represents small fiber branches running perpendicular to the viewing plane, which can also be seen in the corresponding microscopy image. The phase retardance images in Figure 2C indicate that retardance dramatically increases with depth in the white matter, whereas retardance remains low in gray matter. This distinction is more evident in large fiber bundles as shown on the right side of the cross-section (ii), where banding patterns start to appear due to phase wrapping. From visual inspection, the location of peak reflectivity and the position where retardance starts to rise are roughly matched on the same A-line. Figure 2D illustrates the axis orientation images that provide additional information to locate the fiber tracts and distinguish fiber directions in the white matter. Note that phase wrapping in the large fiber tract also alters the axis orientation color in the deeper region, which can be corrected by the software.

The identification of white matter can be more complicated due to its axis-dependent optical characteristics (Hebada et al., 1994). Figure 2E demonstrates a comparison of reflectivity profiles for three distinct neighboring brain regions, which are marked by the color-coded arrows on the cross-sectional images. The internal capsule, indicated by the blue arrow, exhibits the strongest signal in the superficial layer due to the parallel alignment of its component nerve fibers with respect to the viewing plane. On the other hand, the reflectivity profile of the optic tract, in green, is even smaller than that of the gray matter (in red). Therefore, determination of whether a structure is gray or white matter based on the reflectivity information alone from conventional OCT can be misleading. The retardance information provided by the MC-OCT provides a more robust differentiation of the white matter from the gray matter. Figure 2F shows the corresponding retardance curves for these three regions. It is clear that the slope of retardance curves representing the birefringence can be a main indicator of the myelinated nerve fiber tracts.

The attenuation and birefringence are extracted from each A-line for white matter and gray matter regions, and the statistical results are provided in Figure 2G. The reflectivity signal attenuates at $(8.48 \pm 1.46) \times 10^{-2}$ dB/μm in white matter, and $(6.14 \pm 0.88) \times 10^{-2}$ dB/μm in gray matter. Therefore, for conventional OCT images, attenuation may be a better indicator to differentiate the white and gray matter than the peak reflectivity discussed above. The slopes of phase retardance were found to be 0.33 ± 0.10°/μm for white matter and 0.03 ± 0.01 °/μm for gray matter, representing the birefringence of $(7.78 \pm 0.61) \times 10^{-4}$ and $(0.21 \pm 0.068) \times 10^{-4}$, respectively. The values for attenuation and birefringence features are significantly higher for white matter compared to gray matter. However, the differentiation is more pronounced in the birefringence contrast. Thus, birefringence provides a more reliable means of distinguishing myelinated fiber tracts in the brain.

2D brain maps and tractography

En-face images were reconstructed from the MC-OCT cross-sectional images to produce the sagittal view of the rat brain. Figure 3A shows the microscopy image with labeled structures and the reconstructed MC-OCT images. The *en-face* maps of reflectivity, phase retardance and optic axis orientation reveal various features, some of which are apparent only in one map. In addition, sub-surface structures, are visible in *en-face* MC-OCT images, and if desired, the specific structures can be localized in depth using the cross-sectional images. The *en-face* reflectivity map (in Figure 3B) provides clear contour delineation and differentiation of gross structures in the brain which correlate well with the microscope image. In general, the white matter appears brighter than the gray. The dark appearance of the fimbria and the optic tract may be due to the large inclination angle of the fiber axis at the specific location against the viewing plane as discussed in the previous section. As shown in Figure 3C, the phase retardance map highlights the fiber tracts further because the

presence of gray matter is suppressed due to a lack of birefringence. The brightness of the tracts qualitatively provides a sense of axis alignment to the plane. In the internal capsule, small fiber tracts, measuring tens of micrometers in diameter, are clearly visible. Inclined fibers, which might be misinterpreted in the reflectivity map due to their dark appearance, can also be identified. Multiple fiber tracts in the midbrain are visible, and the structural feature of the white matter embedded in the thalamus emerges. The optic axis orientation map in Figure 3D provides further information about the fiber axes. The arrows indicate three groups of fiber tracts with different orientations around the zona incerta. Such detail is not distinguishable in reflectivity and phase retardance maps and is barely detectable using bright-field microscopy. The use of axis orientation information enhances the identification of intermingled fiber tracts running across the viewing plane. An excellent illustration of this feature is the differentiation of internal capsule and optic tract, seen in Figure 3D. Moreover, the MC-OCT contrasts can be combined in order to facilitate better tractography. Figure 3E shows the implementation of 2D tractography by utilizing phase retardance and orientation maps. The axis orientation and the retardance of fibers are encoded by color and brightness of the colors, respectively. The detailed color scheme is illustrated Figure 4J. The spatial organization of the fibers in tractgraphy is in good agreement with the anatomy (F). Based on the brightness and the color of the *en-face* maps, the spatial orientation vector of fibers in the brain may be interpreted.

Comprehensive imaging of the hemisphere was achieved in multiple volume scans. Figure 4 illustrates the course of fiber tracts on the 2D tractography (top panels) and the microscopy images of the corresponding sagittal slices (bottom panels) at four sagittal sections. The HSV color scheme for 2D tractography images is shown in Figure 4J. The *en-face* orientation ($\bar{\theta}$) and retardance ($\bar{\delta}$) images were used to determine colors and brightness of the colors, respectively. Cyan represents a reference direction (0°) for fiber orientation. Since $\bar{\theta}$ is the average axis-orientation along depth, its value may not reach the actual value due to noise and filtering effects. For instance, the maximum deviation ($\bar{\theta}_{max}$) from the reference direction was calculated to be 68°, instead of reaching 90°. Therefore, the colors on the wheel are scaled accordingly. We used en-face retardance $\bar{\delta}$ images to adjust the brightness of colors. As seen along the radial direction of the color wheel, the minimum retardance ($\bar{\delta}$= 0°) yields black and the maximum retardance ($\bar{\delta}$= 60°) represents the full color. For each row panel, the positions of the imaging sections from left to right are indicated by the dashed lines (1–4) on the rat brain (I). The details of fiber tracts are well appreciated in these MC-OCT images. By incorporating optical slices of all sections, white matter distribution and orientation from the lateral to medial sections of the brain may be continuously tracked. More importantly, it is possible to use depth-resolved images to localize the nerve fibers precisely, and track the fibers in 3D.

3D tractography

Three dimensional tractography is created from a single section dataset for a 3D brain volume. Two types of information are encoded in the reconstructed tractography: fiber localization implied by birefringence, and its axis orientation. Figure 5 demonstrates depth localization of fiber tracts in the internal capsule region. The cross-sectional image in Figure 5A shows phase retardance after elimination of speckle noise. The birefringence is derived by taking the pixel-wise slope of the phase retardance. As shown in Figure 5B, the birefringence image allows depth localization of individual fiber bundles within the internal capsule. Considering the discrepancy of the slope values, which may be due primarily to diversity of the fiber inclinations, the fiber bundles are identified as highlighted dots and bands in red, yellow, cyan and light blue. Gray matter is masked in the dark blue background due to the lack of birefringence.

By combining multiple cross-sections, visualization of nerve fibers is achieved in 3D. Volume rendering of the 3D dataset is constructed by the software V3D (Peng et al., 2010). Figure 6 shows optical tractography for a brain volume of $6 \times 6 \times 0.45$ mm^3. HSV color scheme for 3D tractography is shown on the lower right corner of Figure 6. The axis orientation (θ) and birefringence (Δn) of fiber tracts are encoded by colors and brightness of the colors, respectively. Due to noise and filtering effects, the maximum orientation angle (θ_{max}) with respect to the reference direction was 80°, and the θ values on the wheel were scaled accordingly. The brightness of the colors, from black to full color, is controlled by the value of Δn. A white background is selected for better visualization. The nerve fiber tracts are identified by their spatial connections and color. The architecture of tightly packed fiber bundles and the diverse directions of small fiber branches in the internal capsule are visible. The course of small fibers of the commissural stria terminalis are accurately tracked throughout the slice. In addition, some fiber tracts are visible in the deeper regions within the thalamus. The color for a single tract may vary spatially due to change in axis orientation. The color also helps to distinguish neighboring tracts. For example, the oval-shaped optic tract rising from the inferior-posterior brain is clearly differentiated by the color-coded orientation. The fragmented patterns located in the deeper, low SNR regions will likely be visualized better by using more advanced signal processing approaches or a MC-OCT operating at longer wavelength.

Discussion

We used a PMF-based MC-OCT to generate high-resolution 3D images of microstructures and nerve fiber tracking in *ex-vivo* rat brain. We have demonstrated here that MC-OCT imaging with retardance and optic axis orientation contrasts is a valuable method for distinguishing between white and gray matter based on the birefringence property of myelinated axons. This technology enables visualization of nerve fiber tracts that are as small as a few tens of micrometers, and provides comprehensive 3D optical tractography in which unprecedented detail of brain spatial architecture is clearly visible.

Speckle noise, the dominant noise in coherence imaging, needs to be carefully removed in order to enhance image quality. The spatial average of A-lines was commonly adopted in conventional OCT based retinal imaging for speckle reduction. In addition, various digital signal processing algorithms have been demonstrated, including enhanced Lee filter, median filter, symmetric nearest neighbor filter and adaptive Wiener filter (Ozcan et al., 2007). More sophisticated approaches have been proposed for performing filtering in a transform domain, such as wavelet (Adler et al., 2004) and curvelet (Jian et al., 2010). In polarization-sensitive OCT, the effect of speckle noise can be more severe in the retardance and birefringence images. The phase retardance information is typically illustrated in the image; whereas, depth resolved birefringence images which may provide better localization and delineation of anisotropic tissues were rarely utilized, in spite of the fact that it can be calculated from the derivative of retardance. The result, based on the differential operation, is severely degraded by speckle noise. Recently, a coherence-enhancing diffusion filter has been applied to reduce speckle noise in phase retardance images with multiple banding patterns to obtain a stress-induced birefringence distribution (Stifter et al., 2010). Here we used a modified nonlinear diffusion filter to minimize speckle effect in the phase retardance images for localizing nerve fibers in the reconstructed birefringence images. The goal of the nonlinear diffusion filter is to preserve the critical edges of features in the image while reducing speckle noise. As our results indicated, fiber localization in unprecedented detail is realized in 3D, with significantly suppressed speckle effect. One potential problem in the 3D visualization presented here is that some fragmented patches at deeper locations are unidentified, which might be small fibers running into the gray matter structures. Advanced signal processing approaches may show these low SNR regions better. Moreover, a swept

source based imaging system operating at 1300 *nm* wavelength (Al-Qaisi and Akkin, 2010) may allow for improved imaging due to better depth penetration in turbid tissues.

A limitation of MC-OCT is that currently axis orientation of fibers beneath fibers with different orientations is not quantitatively available and phase retardance would not be accurate where multiple layers of fibers are crossing in diverse directions. A quaternion based algorithm has been proposed to distinguish multi-layered local birefringence and optic axis orientations in PS-OCT (Guo et al., 2004). Quantification of depth-resolved axis orientation and birefringence has also been demonstrated in a bulk PS-OCT setup (Kemp et al., 2005). Using the PMF-based MC-OCT technology, more sophisticated models need to be established to achieve better visualization and quantification of depth-dependent axis orientation and phase retardance of fiber tracts in the brain.

As a measure of MC-OCT technique, birefringence can potentially be used as an early indication of pathological changes (Setterfield and Sutton, 1935; Miklossy, and Van der Loos, 1991) in white matter disease, allowing for the detection of fiber atrophy or myelin loss before any morphological deformation is detectable on diffusion MRI. Quantification of birefringence can be obtained from phase retardance acquired by the MC-OCT. However, it should be noted that the influence of inclination angle on phase retardance may confound the interpretation of birefringence changes in the current measures, resulting in an apparent birefringence. A possible solution was proposed using a variable incident angle based polarization-sensitive OCT approach (Ugryumova et al., 2006), in which both tissue birefringence and 3D optic axis orientation can be quantitatively evaluated with series measurements. MC-OCT technology, by providing accurate birefringence data, might be useful for the analysis of neuropathological processes.

With 3D visualization of fiber connection and orientation available, optical tractography has the potential to provide the assessment of diffusion MR images. MR-based diffusion imaging utilizing the anisotropic diffusion of water molecules along fiber tracts allows non-invasive fiber tractography of the human brain. Recent advancement of experimental protocol design and computational models in diffusion imaging techniques have made progress to clarify the ambiguity of crossing fiber tracts within an imaging voxel and obtain reliable connections between the intermingling fiber bundles (Tuch, 2004; Hosey et al., 2005; Wedeen et al., 2008; Tristan-Vega et al., 2009). However, spatial resolution is still limited to a millimeter scale, and the fidelity of the probability-based results needs to be validated by modalities that allow direct access to fiber tracts. Therefore, a cross-validation study comparing diffusion MRI and MC-OCT would be valuable. As the penetration depth of OCT imaging is limited to about 1 mm and even shallower in white matter regions (Jeon et al., 2006), tractography of larger brain regions can be reconstructed *ex-vivo* by stacking slices from multiple MC-OCT volume scans. A combination of MC-OCT and diffusion MRI technologies may open new avenues in the investigation of neurological disorders.

The development of technology that can distinguish white matter, gray matter, and blood vessels via an endoscope would be of significant utility to the neurosurgeon. An endoscopic OCT setup has been proposed for neurosurgical guidance where conventional contrast of scattering was used to differentiate white matter and gray matter (Jafri et al., 2005 and 2009). In spite of some successful identification, it was suggested that the subthalamic nucleus, a primary target for deep brain stimulation (DBS) surgery, was difficult to differentiate from adjacent structures. This difficulty might be overcome by multiple contrasts provided by an endoscopic MC-OCT. Preliminary findings suggest that MC-OCT can detect bi-directional blood flow (data not shown), allowing for the localization of blood vessels in living brain, which could minimize the risk of intracranial hemorrhage — a significant risk in neurosurgical procedures. Thus, development of an endoscopic MC-OCT

technology could provide real-time intraoperative visualization and monitoring, making it potentially useful in clinical applications.

Supplementary Material

Refer to Web version on PubMed Central for supplementary material.

Acknowledgments

This work was supported by the Institute for Engineering in Medicine Seed Grant program at the University of Minnesota and NIH Neuroimaging Training Program (trainee: AJB) T32EB008389.

References

Adler DC, Ko TH, Fujimoto JG. Speckle reduction in optical coherence tomography images by use of a spatially adaptive wavelet filter. Opt Lett. 2004; 29:2878–2880. [PubMed: 15645810]

Al-Qaisi MK, Akkin T. Swept-source polarization-sensitive optical coherence tomography based on polarization-maintaining fiber. Opt Express. 2010; 18:3392–3403. [PubMed: 20389349]

Assaf Y, Pasternak O. Diffusion tensor imaging (DTI)-based white matter mapping in brain research: a review. J Mol Neurosci. 2008; 34:51–61. [PubMed: 18157658]

Axer M, Amunts K, Grässel D, Palm C, Dammers J, Axer H, Pietrzyk U, Zilles K. A novel approach to the human connectome: ultra-high resolution mapping of fiber tracts in the brain. NeuroImage. 2011; 54:1091–1101. [PubMed: 20832489]

Basser PJ, Mattiello J, Le Bihan D. Estimation of the effective self-diffusion tensor from the NMR spin-echo. J Magn Reson B. 1994; 103:247–254. [PubMed: 8019776]

Bürgel U, Mecklenburg I, Blohm U, Zilles K. Histological visualization of long fibre tracts in the white matter of adult human brains. J Brain Res. 1997; 38:397–404.

Burkhalter A, Bernardo KL, Charles V. Development of local circuits in human visual cortex. J Neurosci. 1993; 13:1916–1931. [PubMed: 8478684]

Canny J. A computational approach to edge detection. IEEE Trans Pattern Anal Mach Intell. 1986; 8:679–698. [PubMed: 21869365]

Cense B, Nassif N, Chen T, Pierce M, Yun SH, Park B, Bouma B, Tearney G, de Boer J. Ultrahigh-resolution high-speed retinal imaging using spectral-domain optical coherence tomography. Opt Express. 2004; 12:2435–2447. [PubMed: 19475080]

Catté F, Lions PL, Morel JM, Coll T. Image selective smoothing and edge detection by nonlinear diffusion. SIAM J Numer Anal. 1992; 29:182–193.

Conturo TE, Lori NF, Cull TS, Akbudak E, Snyder AZ, Shimony JS, McKinstry RC, Burton H, Raichle ME. Tracking neuronal fiber pathways in the living human brain. Proc Natl Acad Sci U S A. 1999; 96:10422–10427. [PubMed: 10468624]

de Boer JF, Milner TE, van Gemert MJ, Nelson JS. Two-dimensional birefringence imaging in biological tissue by polarization-sensitive optical coherence tomography. Opt Lett. 1997; 22:934–936. [PubMed: 18185711]

de Campos VB, Mello ML, Caseiro-Filho AC, Godo C. Anisotropic properties of the myelin sheath. Acta Histochem. 1980; 66:32–39. [PubMed: 6776776]

Dorrer C, Belabas N, Likforman JP, Joffre M. Spectral resolution and sampling issues in Fourier transform spectral interferometry. J Opt Soc Am B. 2000; 17:1795–1802.

Götzinger E, Pircher M, Hitzenberger CK. High speed spectral domain polarization sensitive optical coherence tomography of the human retina. Opt Express. 2005; 13:10217–10229. [PubMed: 19503236]

Guo S, Zhang J, Wang L, Nelson JS, Chen Z. Depth-resolved birefringence and differential optical axis orientation measurements with fiber-based polarization-sensitive optical coherence tomography. Opt Lett. 2004; 29:2025–2027. [PubMed: 15455768]

Hebeda KM, Menovsky T, Beek JF, Wolbers JG, van Gemert MJC. Light propagation in the brain depends on nerve fiber orientation. Neurosurgery. 1994; 35:720–724. [PubMed: 7808616]

Hosey T, Williams G, Ansorge R. Inference of multiple fiber orientations in high angular resolution diffusion imaging. Magn Reson Med. 2005; 54:1480–1489. [PubMed: 16265642]

Huang D, Swanson EA, Lin CP, Schuman JS, Stinson WG, Chang W, Hee MR, Flotte T, Gregory K, Pufialito CA, Fujimoto JG. Optical coherence tomography. Science. 1991; 254:1178–1181. [PubMed: 1957169]

Jafri MS, Farhang S, Tang RS, Desai N, Fishman PS, Rohwer RG, Tang CM, Schmitt JM. Optical coherence tomography in the diagnosis and treatment of neurological disorders. J Biomed Opt. 2005; 10:051603. [PubMed: 16292951]

Jafri MS, Tang R, Tang CM. Optical coherence tomography guided neurosurgical procedures in small rodents. J Neurosci Methods. 2009; 176:85–95. [PubMed: 18838087]

Jeon SW, Shure MA, Baker KB, Huang D, Rollins AM, Chahlavi A, Rezai AR. A feasibility study of optical coherence tomography for guiding deep brain probes. J Neurosci Methods. 2006; 154:96–101. [PubMed: 16480773]

Jian Z, Yu L, Rao B, Tromberg BJ, Chen Z. Three-dimensional speckle suppression in optical coherence tomography based on the curvelet transform. Opt Express. 2010; 18:1024–1032. [PubMed: 20173923]

Kemp NJ, Zaatari HN, Park J, Rylander HG III, Thomas M. Depth-resolved optic axis orientation in multiple layered anisotropic tissues measured with enhanced polarization-sensitive optical coherence tomography (EPS-OCT). Opt Express. 2005; 13:4507–4518. [PubMed: 19495365]

Lanciego JL, Wouterlood FG. Neuroanatomical tract-tracing methods beyond 2000: what's now and next. J Neurosci Meth. 2000; 103:1–2.

Larsen L, Griffin LD, GrÄβel D, Witte OW, Axer H. Polarized light imaging of white matter architecture. Microsc Res Tech. 2007; 70:851–863. [PubMed: 17661367]

Leitgeb R, Hitzenberger C, Fercher A. Performance of Fourier domain vs. time domain optical coherence tomography. Opt Express. 2003; 11:889–894. [PubMed: 19461802]

Lichtman JW, Live J, Sanes JR. A technicolour approach to the connectome. Nat Rev Neurosci. 2008; 9:417–422. [PubMed: 18446160]

Miklossy J, Van der Loos H. The long-distance effects of brain lesions: visualization of myelinated pathways in the human brain using polarizing and fluorescence microscopy. J Neuropath Exp Neur. 1991; 50:1–15. [PubMed: 1702142]

Nakaji H, Kouyama N, Muragaki Y, Kawakami Y, Iseki H. Localization of nerve fiber bundles by polarization-sensitive optical coherence tomography. J Neurosci Methods. 2008; 174:82–90. [PubMed: 18675301]

Ozcan A, Bilenca A, Desjardins AE, Bouma BE, Tearney GJ. Speckle reduction in optical coherence tomography images using digital filtering. J Opt Soc Am A. 2007; 24:1901–1910.

Park BH, Pierce MC, Cense B, Yun SH, Mujat M, Tearney GJ, Bouma BE, de Boer JF. Real-time fiber-based multi-functional spectral-domain optical coherence tomography at 1.3 μm. Opt Express. 2005; 13:3931–3944. [PubMed: 19495302]

Paxinos, G.; Watson, C. The Rat Brain in Stereotaxic Coordinates. 6. Elsevier Inc. (Academic Press); 2007.

Peng H, Ruan Z, Long F, Simpson JH, Myers E. V3D enables real-time 3D visualization and quantitative analysis of large-scale biological image data sets. Nat Biotechnol. 2010; 28:348–353. [PubMed: 20231818]

Perona P, Malik J. Scale space and edge detection using anisotropic diffusion. IEEE Trans Pattern Anal Mach Intell. 1990; 12:629–639.

Setterfield HE, Sutton TS. The use of polarized light in the study of myelin degeneration. Anat Rec. 1935; 61:397–411.

Stifter D, Leiss-Holzinger E, Major Z, Baumann B, Pircher M, Götzinger E, Hitzenberger CK, Heise B. Dynamic optical studies in materials testing with spectral-domain polarization-sensitive optical coherence tomography. Opt Express. 2010; 18:25712–25725. [PubMed: 21164917]

Tristan-Vega A, Westin CF, Aja-Fernandez S. Estimation of fiber orientation probability density functions in high angular resolution diffusion imaging. NeuroImage. 2009; 47:638–650. [PubMed: 19393321]

Tuch DS, Reese TG, Wiegell MR, Makris N, Belliveau JW, Wedeen VJ. High angular resolution diffusion imaging reveals intravoxel white matter fiber heterogeneity. Magn Reson Med. 2002; 48:577–582. [PubMed: 12353272]

Tuch DS. Q-ball imaging. Magn Reson Med. 2004; 52:1358–1372. [PubMed: 15562495]

Ugryumova N, Gangnus SV, Matcher SJ. Three-dimensional optic axis determination using variable incidence-angle polarization-optical coherence tomography. Opt Lett. 2006; 31:2305–2307. [PubMed: 16832467]

Wang H, Al-Qaisi MK, Akkin T. Polarization-maintaining fiber based polarization-sensitive optical coherence tomography in spectral domain. Opt Lett. 2010; 35:154–156. [PubMed: 20081952]

Wedeen VJ, Wang RP, Schmahmann JD, Benner T, Tseng WYI, Dai G, Pandya DN, Hagmann P, D'Arceuil H, de Crespigny AJ. Diffusion spectrum magnetic resonance imaging (DSI) tractography of crossing fibers. NeuroImage. 2008; 41:1267–1277. [PubMed: 18495497]

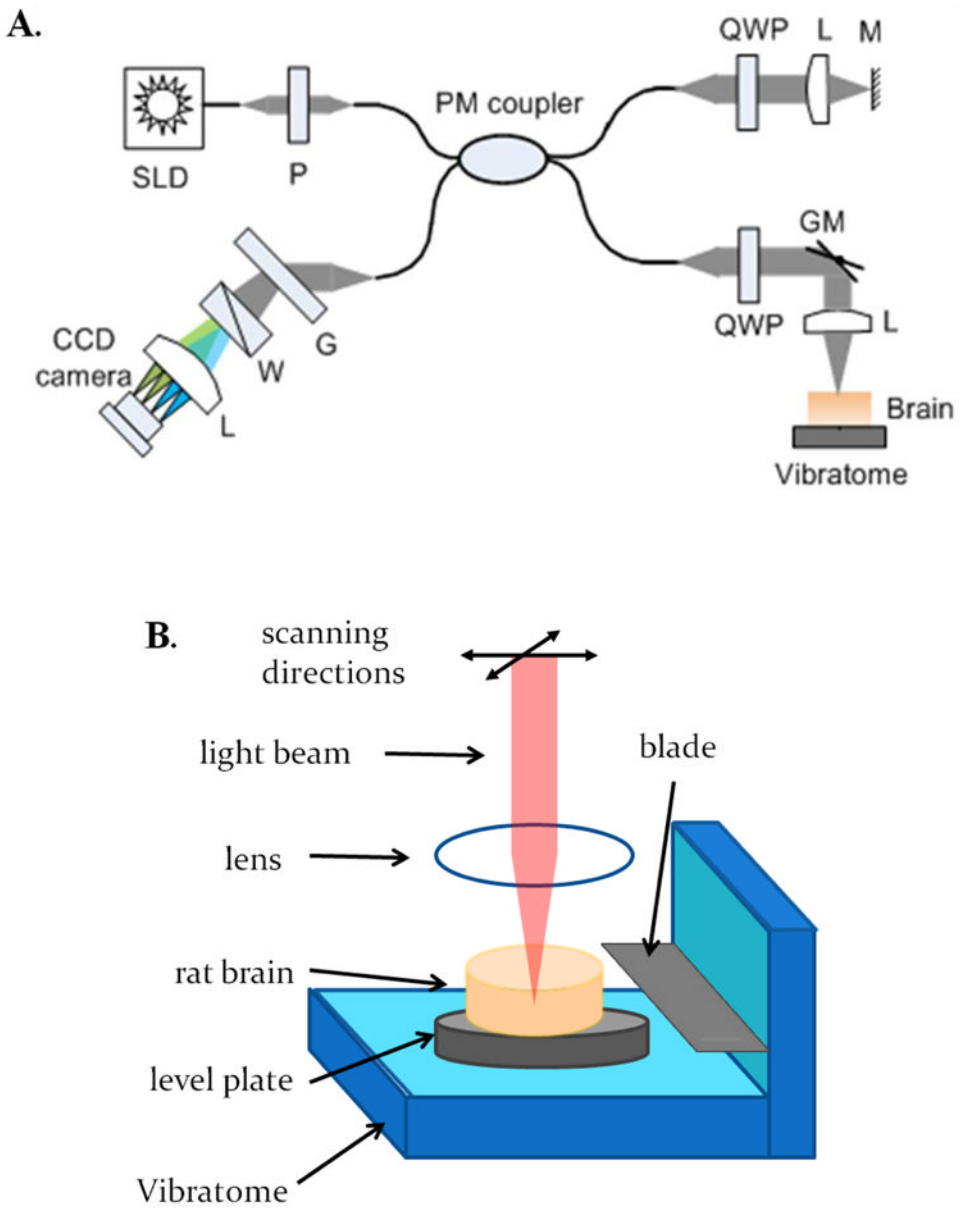

Figure 1.

MC-OCT setup for brain imaging. (A) System schematic diagram. SLD, superluminscent diode; FB, fiber bench; P, polarizer; C, collimator; QWP, quarter-wave plate; L, lens; M: mirror; GM, galvo mirror; G, grating; W, Wollaston prism. (B) Experimental configuration under sample arm. The brain sample is mounted on a Vibratome slicer, which is placed under the sample arm optics that scans the beam over the tissue.

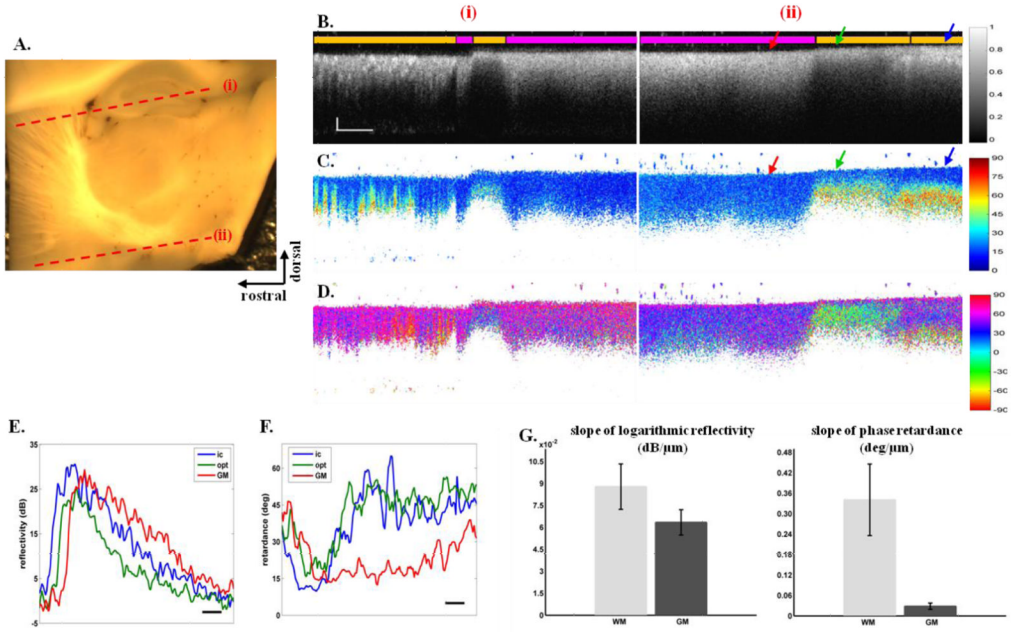

Figure 2.

Microscopy and cross-sectional MC-OCT images of an *ex-vivo* rat brain. Microscopy image (A) demonstrates a sagittal section of the right hemisphere. Cross-sectional MC-OCT images of reflectivity (B), phase retardance (C) and optic axis orientation (D) are shown for two cross-sections (i and ii) indicated by the dashed lines on A (scale bars: 100 μm axial, 500 μm lateral). White and gray matter regions are marked by orange and pink bars on top of the reflectivity images. Color-coded arrows on cross-section ii indicate white matter regions with small (blue) and large (green) inclination angles, and the adjacent gray matter region (red). Reflectivity and phase retardance profiles of six A-line averages for these regions are shown in E and F (scale bar: 50 μm). Mean and standard deviations of attenuation and birefringence for white and gray matter are shown in G.

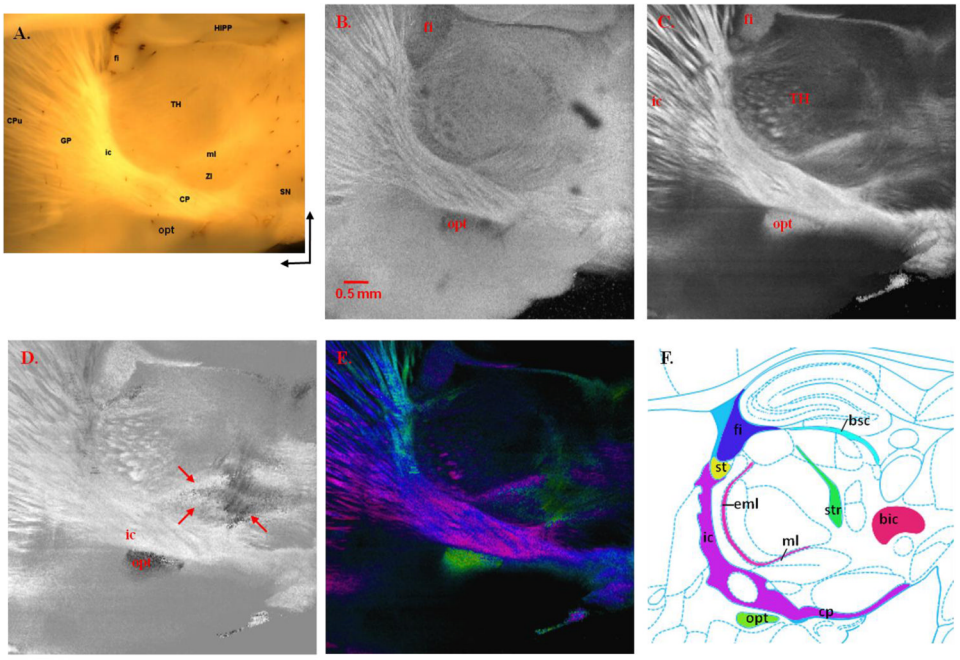

Figure 3.

Microscopy image (A) and reconstructed MC-OCT *en-face* images (B–D) of a sagittal rat brain section, with comparison of anatomy (F). Structures are labeled on the microscope image (A): cp- cerebral peduncle; CPu- caudate putamen; fi- fimbria; GP- globus pallidus; HIPP- hippocampus; ic- internal capsule; ml- medial lemniscus; opt- optic tract; SN- substania nigra; TH- thalamus; ZI- zona incerta. Leftward arrow: cranial; upward arrow: dorsal. Reconstructed brain maps of reflectivity (B), phase retardance (C), optic axis orientation (D) and combined image for tractography (E) are shown. The color map of E is illustrated in Figure 4J. The arrows in D indicate three groups of fiber bundles with different orientations. The image in F is modified from The Rat Brain in Stereotaxic Coordinates (Paxinos and Watson, 2007) with permission. Abbreviations of structures: bic- brachium of the inferior colliculus; bsc- brachium of the superior colliculus; cp- cerebral peduncle; eml- external medullary lamina; fi- fimbria; ic- internal capsule; ml- medial lemniscus; opt- optic tract; st- stria terminalis; str- superior thalamic radiation.

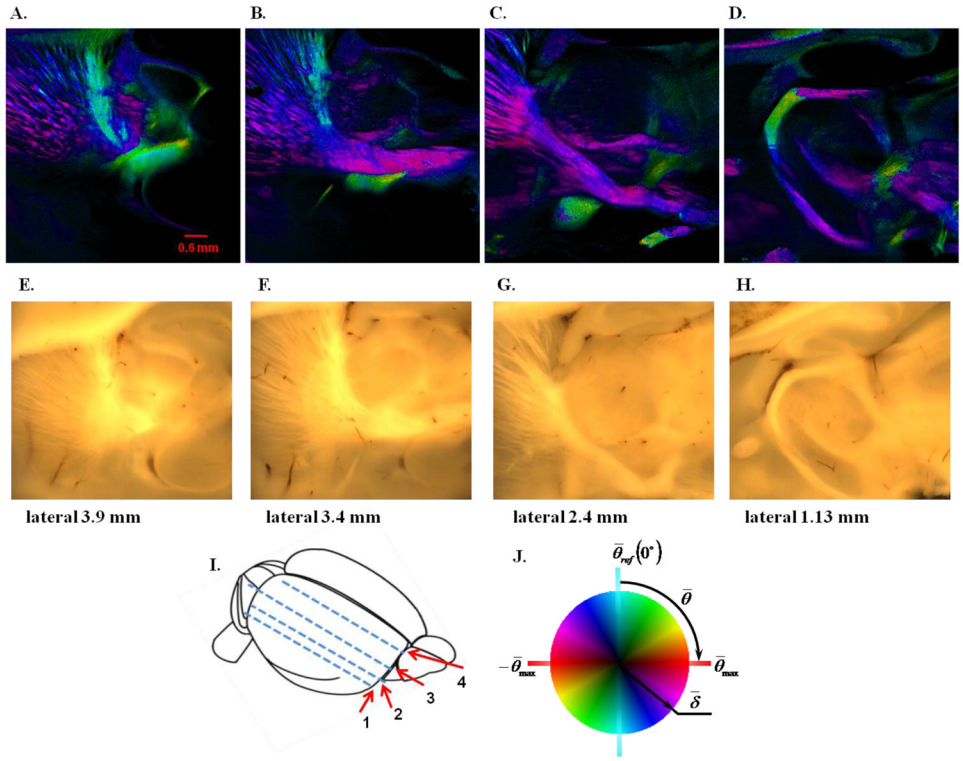

Figure 4.

2D tractography of the right hemisphere of the rat brain for four sagittal sections (A, B, C, D) and corresponding microscope images (E, F, G, H). The four locations of the images from left to right are lateral 3.9 mm, 3.4 mm, 2.4 mm and 1.13 mm, which are indicated by the dashed lines (1–4) on the right hemisphere of rat brain (I), respectively. The color scheme of tractography images is shown in J. The *en-face* orientation and retardance of fiber tracts determine the color and brightness of the images, respectively.

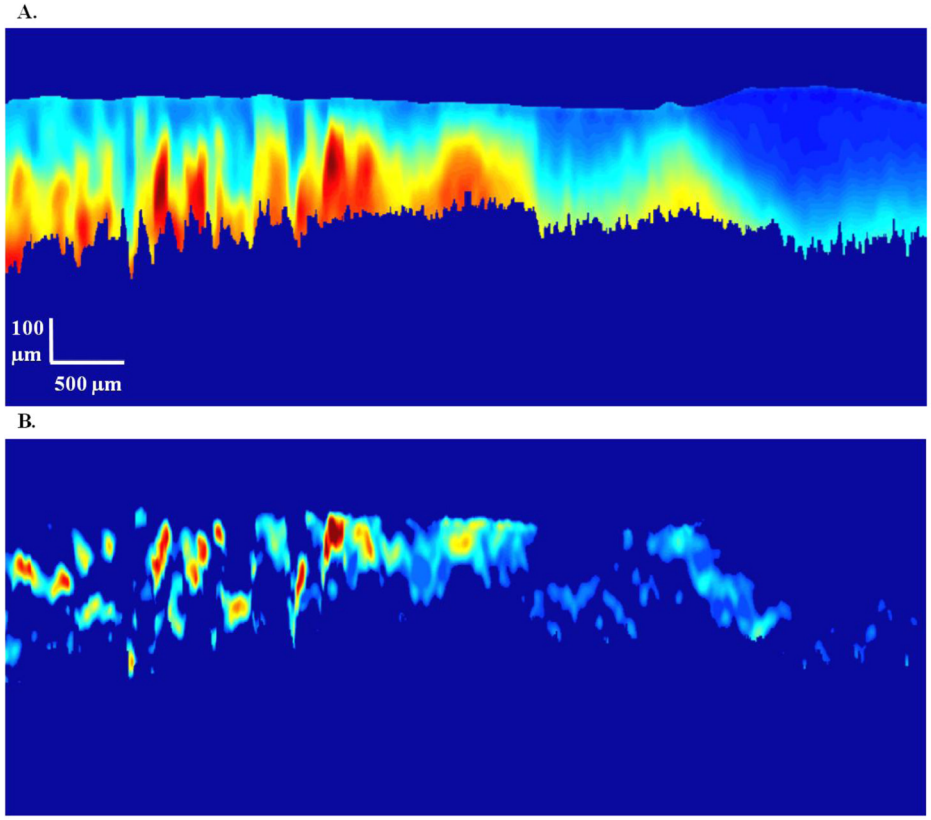

Figure 5.
Depth localization of fiber tracts in the internal capsule of the rat brain. Cross-sectional phase retardance image after speckle reduction (A) is used to obtain the birefringence image (B) that shows nerve fibers at particular depths. White matter is illustrated in red, yellow, cyan and light blue in B, and gray matter is masked in the dark blue background due to the lack of birefringence.

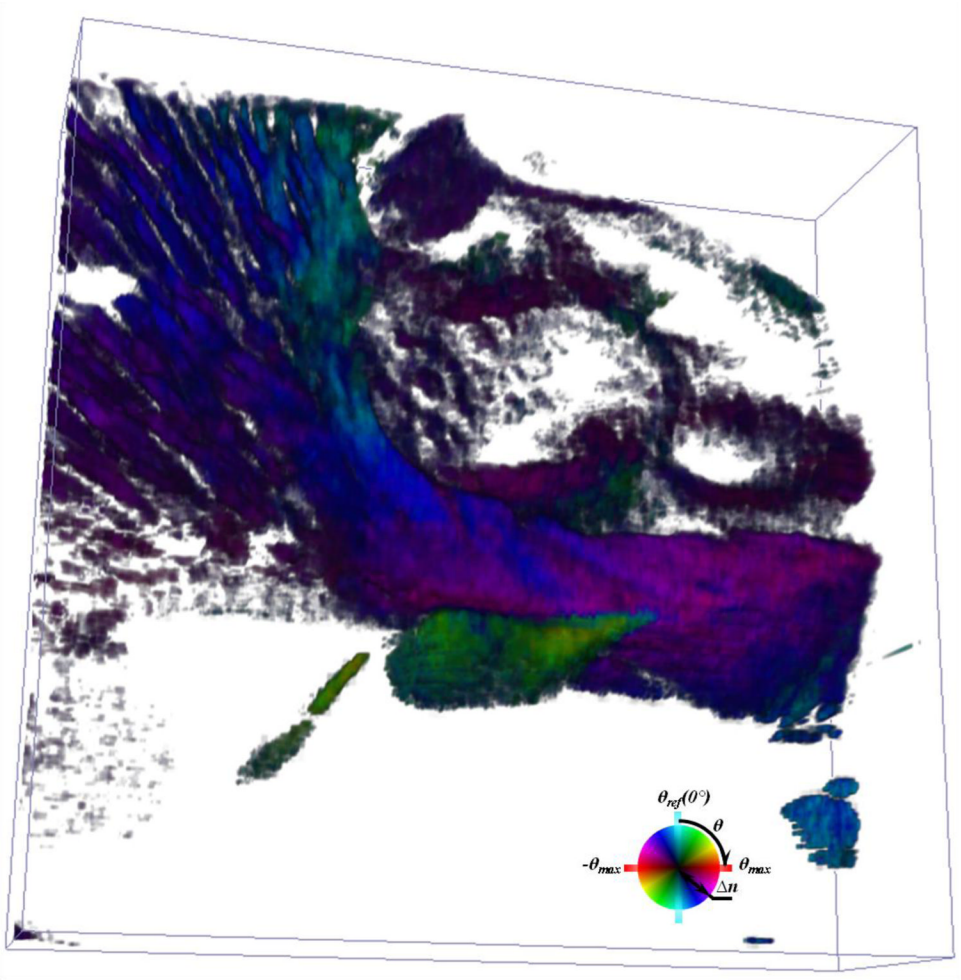

Figure 6.
3D optical tractography of a rat brain section (brain volume: 6 × 6 × 0.45 mm^3). The color scheme is given on the lower right corner. Nerve fibers are continuously tracked and presented in different colors which indicate their axis orientations θ, and the brightness of colors is controlled by the birefringence Δn (See also a movie in the supplemental material).